Generalized Scatter Correction Method in SPECT Using Point Scatter Distribution Functions

Peter Msaki, Bertil Axelsson, C. Magnus Dahl, and Stig A. Larsson

Department of Radiation Physics, Karolinska Institute, Department of Hospital Physics, Karolinska Hospital, Stockholm, Sweden

A new two-dimensional (2-D) scatter correction technique in single photon emission computed tomography (SPECT) based on convolution or frequency filtering with a 2-D scatter distribution function is described. A scatter distribution function of the form A exp(−Br), has been derived from measurements of a point source in a water phantom. Both the amplitude A and the slope B of this function, were approximately invariant with source position except near phantom surface. The accuracy of the 2-D correction technique was compared with that of the previous one-dimensional (1-D) scatter correction technique. As could be expected the latter technique was shown to be less accurate due to its dependence on axial distribution of radioactivity. Phantom SPECT studies showed a clear superiority of the 2-D over the 1-D scatter correction in quantitative imaging. Images derived from clinical studies of regional bloodflow with ^{99m}Tc-HM-PAO and liver uptake showed significant contrast improvement by both techniques.

J Nucl Med 28:1861–1869, 1987

Scattered photons may produce large fractions of falsely positioned events in conventional scintigraphic imaging as well as in single photon emission computed tomography (SPECT). These unwanted events introduce a low-frequency blurring which reduces image contrast and hence, lesion detectability in qualitative imaging. In quantitative imaging, the presence of scattered events can introduce large errors in the assessment of regional radionuclide concentrations (*1,2*).

An early approach to reduce the deteriorating effects of scattered events on scintigraphic images was to raise the lower threshold of the energy discrimination window to the upper part of the total absorption peak (*7–9*). While this method is also appropriate to SPECT, it has serious disadvantages—the fraction of scattered photons will still be disturbingly high while the number of primary events may be reduced to such a degree that the resulting image noise omits both qualitative and quantitative evaluation.

More recently developed scatter correction techniques are based upon subtraction of events in a proportion that corresponds to the actual distribution of scattered events in the acquired images. The amount and distribution of scattered photons may be obtained by Monte-Carlo simulations or by some other mathematic modeling (*3–6*), by acquiring scattered events in a separate energy discrimination window (*7–10*) or by convolving the acquired images with some experimentally derived scatter distribution function (*11–15*). Calculation of the scatter content in images by such convolution or frequency filtering has previously been described using line spread scatter functions (*12*). However, if high accuracy should be achieved by this method, the length of the line source has to match the extension of the radioactive distribution in axial direction.

In this work, a more generalized scatter correction technique is proposed for SPECT. This new method is based on filtering by two-dimensional (2-D) convolution in the spatial domain or frequency filtration in the Fourier domain, of acquired images with a 2-D scatter distribution function that takes into account the scatter contribution from the global distribution of radioactivity in the object under examination.

MATERIALS AND METHODS

Theory

The limited energy resolution of current gamma cameras, inevitably leads to detection of a mixture of scattered and

Received Dec. 2, 1986; revision accepted June 15, 1987.

For reprints contact: P. Msaki, Dept. of Radiation Physics, Karolinska Institute, S-104 01 Stockholm, Sweden.

primary events which are indistinguishable after acquisition. Thus, a removal of scatter contribution from the images obtained using a single energy discrimination window—set to cover the total absorption peak—has to rely on some kind of scatter distribution function that relates the scatter content to the total amount of photons in the matrix of acquired events. The number of events "t" in any pixel of such an image matrix may therefore be considered as a mixture of primary "p" and scattered "s" events according to the sum:

$$t_{i,j} = p_{i,j} + s_{i,j} \tag{1}$$

where, respectively, the indices i, j label the row and the column of a pixel (i, j) in the N × N image matrix; i, j = 1,2, . . ., N. A fraction Δs_{ij} of the scattered events $s_{i,j}$ that has been registered in this pixel may furthermore be related to the number of recorded primary events $P_{u,v}$, in a pixel at position (u, v) of the matrix such that:

$$\Delta s_{i,j}(u,v) = p_{u,v} \cdot q(r_{i-u,j-v}), \tag{2}$$

where q(r) represents some scatter distribution function and $r_{i-u,j-v}$ is the distance between the pixels (i, j) and (u, v), respectively. By summing the scatter contributions from each position of the entire matrix, the total amount of scattered events in the pixel at position (i, j) may be expressed:

$$s_{i,j} = \sum_{u=1}^{n} \sum_{v=1}^{M} \Delta s_{i,j}(u,v) = \sum_{u=1}^{n} \sum_{v=1}^{M} p_{u,v} \cdot q(r_{i-u,j-v}).$$

Using the result in Eq. (1) leads to:

$$t_{i,j} = p_{i,j} + \sum_{u=1}^{n} \sum_{v=1}^{M} p_{u,v} \cdot q(r_{i-u,j-v}), \tag{3}$$

which, in matrix denotation can be expressed as:

$$T = P + P \otimes\otimes Q \tag{4}$$

where the symbol (⊗⊗) denotes a 2-D convolution. We would like to obtain the matrix P of primary events from the matrix T of acquired events. This can be done by first performing a 2-D Fourier transformation of Eq. (4):

$$\mathcal{F}(T) = \mathcal{F}(P + P \otimes\otimes Q) = \mathcal{F}(P) + \mathcal{F}(P) \cdot \mathcal{F}(Q)$$

and rearranging the terms to:

$$\mathcal{F}(P) = \frac{\mathcal{F}(T)}{1 + \mathcal{F}(Q)}. \tag{5}$$

Finally b performing an inverse Fourier transformation of Eq. (5), we obtain the desired matrix P of the primary events:

$$P = T \otimes\otimes \mathcal{F}^{-1} \left\{ \frac{1}{1 + \mathcal{F}(Q)} \right\}. \tag{6}$$

Eq. (5) can be solved in the Fourier domain when both (T) and (Q) are known. Alternatively, it can be solved in the spatial domain by expanding the term inside the brackets:

$$\begin{aligned} P &= T \otimes\otimes \mathcal{F}^{-1} \left\{ \frac{1}{1 + \mathcal{F}(Q)} \right\} \\ &= T \otimes\otimes \mathcal{F}^{-1} \{1 - \mathcal{F}(Q) + [\mathcal{F}(Q)]^2 - [\mathcal{F}(Q)]^3 + \cdots\} \qquad (7) \\ &= T \otimes\otimes \{\delta - Q + Q \otimes\otimes Q - Q \otimes\otimes Q \otimes\otimes Q + \cdots\}, \end{aligned}$$

where δ is the unit impulse function. According to Eq. (7) the matrix P can be obtained from the acquired matrix T provided that a suitable scatter distribution function (matrix) Q can be found.

Scatter Distribution Function Q

There are various alternatives for obtaining a suitable scatter distribution function, including Monte-Carlo simulations and phantom measurements. Previously, an experimentally evaluated one-dimensional (1-D) scatter distribution function was used for scatter correction in a number of cases (*12–14*).

In this work, a new experimentally derived (2-D) scatter distribution function is introduced. This function was obtained from measurements of a point source in water and its normalization was carried out using measurements made in air. The nature of the function obtained permitted an exponential description of the form:

$$Q(r) = A \exp(-Br), \tag{8}$$

where A and B are experimentally determined scatter constants and r represents the radial distance measured from the point corresponding to the location of the point source on the image matrix.

EXPERIMENTAL PROCEDURES

SPECT System, Acquisition, and Reconstruction

The SPECT system used in this work, consisted of a gamma camera 400 ACT* supplied with a low-energy, all-purpose (LEAP) collimator. The energy resolution (whole field of view) of the detector was 12% for ^{99m}Tc. A 20% energy discrimination window, centered at the 140 keV photo-peak of ^{99m}Tc, was used in all experiments. The gamma camera was connected on-line to a PDP11/34, operating with Gamma 11 and the Karolinska Hospital soft-ware (SPETS) (*16*). Both planar and SPECT imaging were performed using 64 × 64 acquisition matrix. In experiments with large phantoms (diameter Ø = 300 mm) the matrix was adjusted over the whole field-of-view (Ø = 400 mm), thus giving a pixel size of 6.3 × 6.3 mm². In experiments conducted with smaller phantoms (Ø = 220 mm), the matrix was zoomed to cover a square detector area of 260 × 260 mm² and a pixel size of 4.1 × 4.1 mm². All SPECT examinations were made with 64 or 128 angles and an acquisition time of 10–15 sec per angle. The radius of rotation used in phantom studies was 150 mm.

All reconstructions were performed by filtered backprojection using modified versions of the Shepp-Logan filter selected from the variety of filters implemented in the software (*16*). The optional algebraic postreconstruction attenuation correction produce (AT2) in the software was applied to all SPECT studies. Attenuation correction was performed on scatter corrected images using the attenuation coefficient $\mu = 0.15$ cm^{-1} reported for "narrow beam geometry" (*17*). In cases where scatter correction was not done, correction for attenuation was performed using empirical attenuation constants obtained from transmission measurements.

Point Spread Functions

Point spread functions were evaluated from measurements of a small cylindrical technetium-99m (^{99m}Tc) source (diameter and height 3 mm) in a water-filled cylindrical phantom of diameter 220 mm and height 200 mm. The water phantom was positioned with its central axis parallel to the collimator plane at a distance of 160 mm from the collimator surface. The variability of the point scatter distribution function with position was analyzed by positioning the source, in steps, along two orthogonal directions in parallel and in perpendicular direction to the collimator plane. Point-spread functions in the direction perpendicular to the collimator plane were obtained at equidistant positions 0, ±30, ±50, ±65, ±75, ±90 mm from the center of the phantom in order to permit averaging by the geometric mean in accordance with the SPECT reconstruction procedure. The positive and negative signs indicate distances, as measured from the center towards (+) and away (−) from the collimator surface, respectively. Similar measurements were made along the direction parallel to the collimator plane at 15, 25, 45, 60, 75, and 90 mm from the center of the phantom. At each position of the source, repeated measurements were performed with the source in air in order to estimate the primary photon (mainly) content (after attenuation correction) of the previous water measurements. All these measurements were conducted in zoom mode.

Evaluation of Scatter Distribution Function

Prior to scatter correction, opposed views of SPECT acquisition data were averaged by the geometric mean. Therefore, all evaluations of scatter distribution functions were made after forming the geometric mean (pixel by pixel) of opposed projected views of the source. An example of a point spread function thus obtained is presented in Figure 1. The shape of these functions in log-lin scale permitted a straight-line fitting to each "wing" of the function by linear regression. Each pair of lines were extrapolated to form an intersection that corresponds to the location of the point source. The number of scattered events N_0 associated with the point of intersection, was divided by the total number of primary events (corrected for decay, attenuation and acquisition time) of the air measurement at corresponding position. The ratio obtained by this normalization denotes the scatter amplitude "A". The average value of the slopes of the left and right straight lines produced a second scatter constant, "B". Usually, due to factors such as curvature and length of cylindrical phantoms, the scatter distribution function for a given phantom is not symmetrical and this assymmetry increases as the phantom surface is approached. In the assessment of the complete scatter distribution function according to Eq. (8) an averaged function was obtained from the vertical and horizontal scatter distribution function each evaluated as described above.

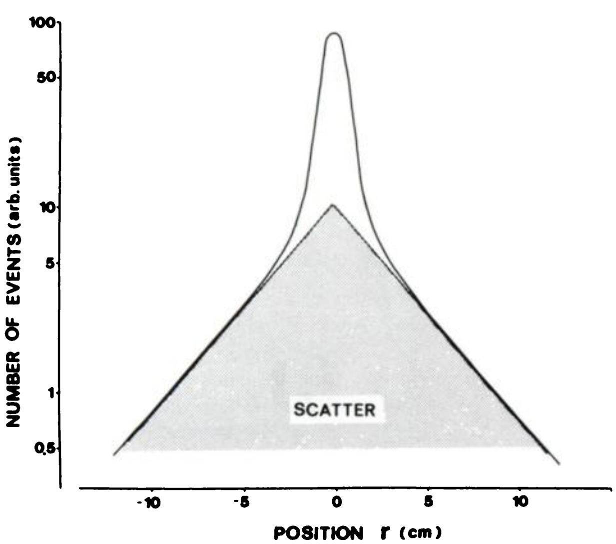

FIGURE 1
Point spread function (solid line) on a semilog scale. The fitted dashed—straight lines are used in the evaluation of the amplitude A (events at the point of intersection, normalized to the total number of primary events) and the slope B (decrease in number of events per unit distance of the scatter distribution function $Q(r) = A \exp(-Br)$.

Filter Design and Its Operation

The scatter constants A and B were used, according to Eq. (8), to establish the scatter distribution function Q required for the implementation of a 2-D IIR (Infinite-duration Impulse Response) filter. This filter is represented by the series expansion ($\delta - Q + Q \otimes\otimes Q - Q \otimes\otimes Q \otimes\otimes Q + \ldots$) term of Eq. (7). All scatter distribution functions in this work have lead to series expansions which satisfied the convergence conditions given by Dudgeon and Mersereau (*18*). A 2-D matrix of 31 by 31 points was selected as a compromise between accuracy in scatter estimations and short computation time. This choice, however, excludes all points that would contribute by 5 per cent or less of the maximum value of the convolving matrix using ^{99m}Tc and a pixel-size 6.3×6.3 mm^2. Filter implementations were always based on the first nine terms of the series of Eq 7. The maximum value of the ninth term used was always ≤1% of the maximum value of the first term. The filter subsequently used in the 2-D scatter correction and some of its associated first nine terms are shown in Figure 2. The 2-D scatter corrections were effected by convolving each image projection matrix T with the filter, constructed in tabulated matrix form, point by point in section after section, according to Eq. (7) and Figure 3.

Comparison of 1-D and 2-D Scatter Correction

The 1-D scatter correction technique used previously has, in general, relied on a scatter distribution function derived from a single line source of specific length, for instance, 100 mm (*12,13*) Figure 4.

The 1-D scatter distribution functions from line sources of various length (including 100 mm long source) were investigated from measurements made using a larger cylindrical (diameter 300 mm and height 200 mm) phantom. This phantom was filled with water and positioned with its central axis parallel to the collimator plane at a distance 210 mm from the collimator surface. The length of the line sources used varied from 5 mm to 150 mm and each source was, in turn, positioned along the central axis of the phantom and planar images of the sources were acquired in normal mode. The scatter distribution functions were evaluated from the line-spread functions obtained, for both experiments, as described earlier by Axelsson (*12*).

The 1-D scatter correction function used for the comparative SPECT-studies of this work, was evaluated from the line-spread function of a 100 mm long cylindrical (diameter 3 mm) line source. The source was positioned along the central axis of the same cylindrical (diameter and height = 200 mm) water-filled phantom as was later used in the SPECT measurements described below. The phantom was positioned with its central axis parallel to the collimator plane. In this case,

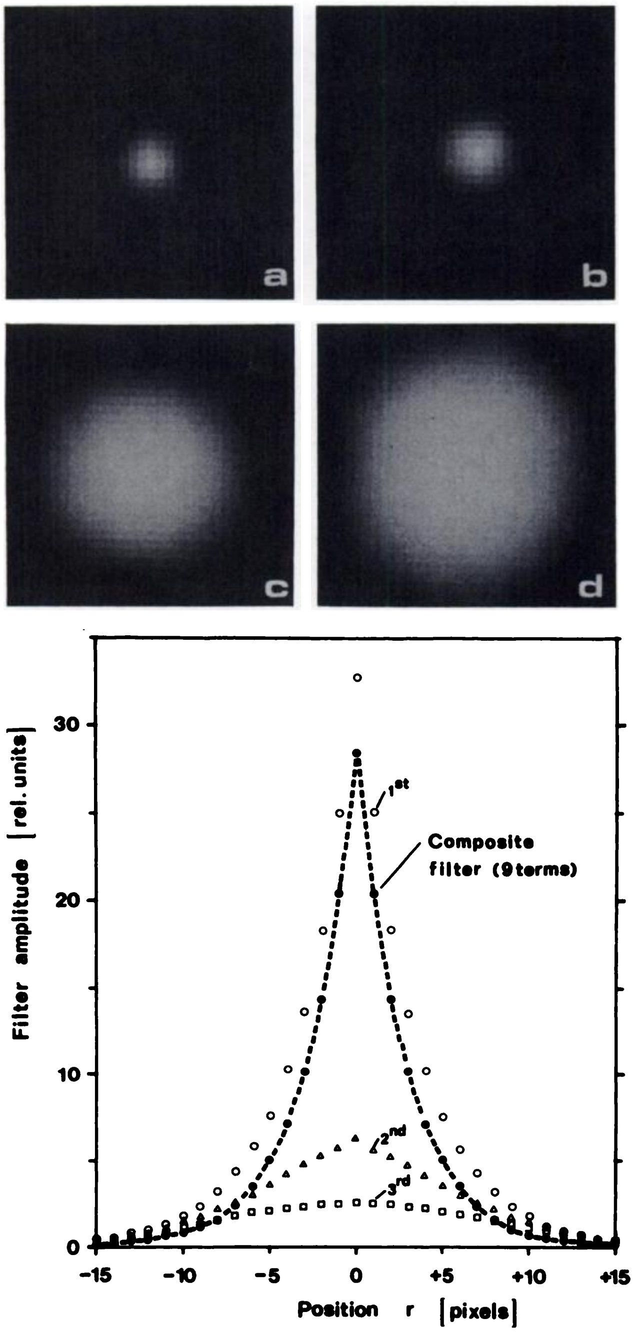

FIGURE 2
Top: The composite 2D-filter function (a) and its first three components, b, c, and d, respectively. Bottom: The amplitude of the filter function and its first three components.

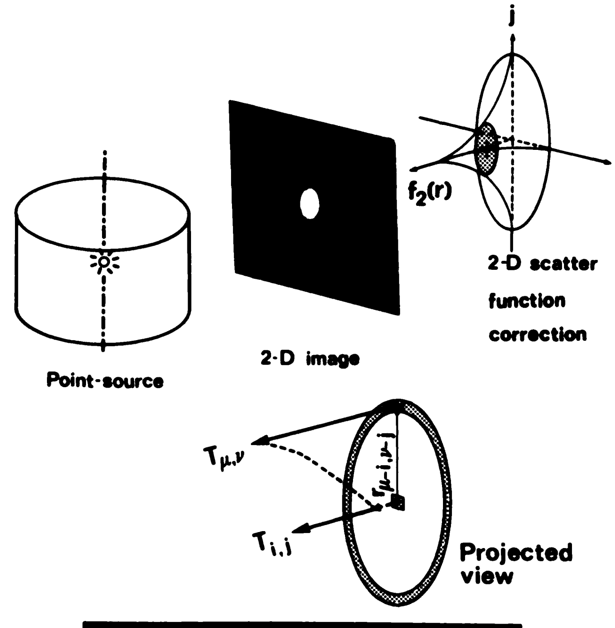

$$P_{i,j} = T_{i,j} - \sum_{\mu=1}^{M}\sum_{\nu=1}^{N} T_{\mu,\nu}\, f_2(r_{\mu-i,\nu-j})$$

FIGURE 3
Principles of 2-D scatter correction illustrating the source—image relation used to obtain the scatter distribution function Q for the correction filter (f_2) (above) and its implementation in the 2-D scatter correction (below).

the planar acquisitions of line spread functions were performed in zoom mode.

Five SPECT studies were conducted to compare the quantitation accuracy for the 1-D and 2-D method with varying axial extension of the radioactive distribution. These measurements were performed with the smaller phantom (Ø = 200 mm). This phantom had a 30 mm water-filled layer surrounding an inner cylindrical volume of diameter 140 mm. The latter volume was further divided in three different transverse segments by means of two circular lucite plates. The axial length of these segments, was varied by changing the position of the plates. The details of the phantom are shown in Figure 5. In all the five SPECT studies, the upper and the lower segments were filled with water while the variation of radioactive distributions used in these studies took place in the middle segment.

Two uniform ^{99m}Tc radioactive solutions of different concentrations, i.e., 100 and 20 kBq/ml, were used. Four small cylinders, each of diameter 40 mm and lengths 25, 50, 75, and 100 mm, respectively, were filled with the 20 kBq/ml solution. They were then positioned, in turn, in the middle segment in such a way that their axes were parallel with the axis of the phantom. The middle segment was adjusted to the length of the cylinder inserted using the circular lucite plates. The rest of the middle segment was then filled with the 100 kBq/ml solution which surrounds this cylinder as shown in Figure 5.

A calibration SPECT measurement, which was used to convert the previous measurement values (events per pixel) into concentration (kBq/ml) values, was conducted with a 100 mm long middle segment filled with the 100 kBq/ml uniform solution.

CLINICAL EXAMINATIONS

The 2-D scatter correction technique is presently being introduced clinically: for instance, in studies of regional brain blood-flow with [^{99m}Tc]HM-PAO and in detection of space occupying lesions of the liver and the spleen (*19*). In the brain

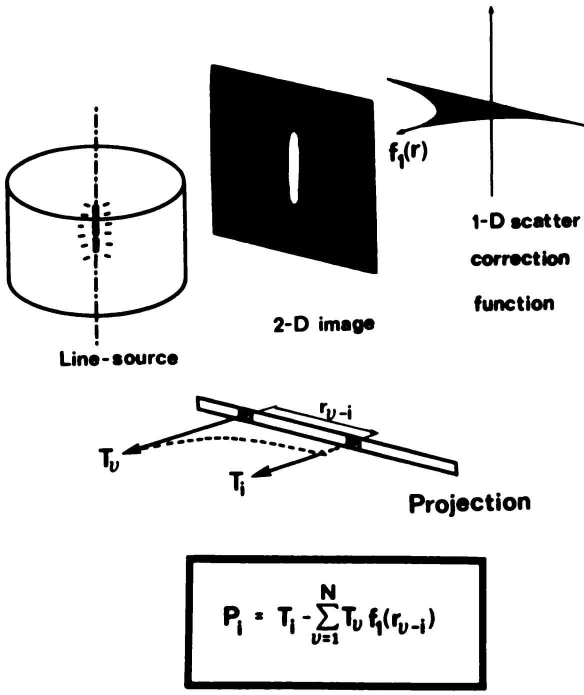

FIGURE 4
Principles of 1-D scatter correction illustrating the source—image relation used to establish the distribution function (f_1) (above) and its implementation in the 1-D scatter correction (below).

blood-flow studies tomographic acquisitions (with 128 angle and acquisition time of 15 sec per angle, pixel size 4.1 mm^2) are performed 10–15 min after i.v. injection of 500 MBq [^{99m}Tc]HM-PAO. The liver-spleen scintigraphy (64 angles, 15 sec per angle, pixel size 6.3 mm^2) is performed 5–10 min after injection of 120 MBq [^{99m}Tc]albumin colloid (ALBU-RES). Reconstructions were performed from both uncorrected and corrected projections.

RESULTS

Comparison Between 1-D and 2-D Scatter Correction Techniques

The variation of the 1-D scatter distribution function with length of the line-source is demonstrated in Figure 6. As seen in this figure, the 1-D scatter distribution function depends strongly (almost exclusively through the scatter amplitude) on source length. This dependence is very important for short sources and moderate for sources longer than 140 mm.

The behavior of the 2-D scatter distribution function with source position within the phantom, in terms of the scatter amplitude A, and slope B, is demonstrated in Figures 7 and 8. According to Figure 7, both the scatter amplitude and the slope are constant along the lateral axis of the skull phantom, except for the slightly increased values observed in the region close (within 30–40 mm) to the phantom surface.

The variation of the scatter function constants with depth, as measured from the phantom surface (on the axis perpendicular to the collimator surface), is presented in Figure 8. According to this figure, the scatter amplitude is independent of depth at all positions except in regions closer than 30–40 mm to the surface of the phantom. At shallower depths, the amplitude decreases very rapidly as the phantom surface is approached while the slope is observed to deviate as much as 30% (from 0.19 to 0.26) of the central value.

For the SPECT phantom studies, comparisons were made between concentration values obtained from uncorrected 1-D and 2-D scatter corrected sections, respectively. In each case, the average number of registered events per pixel was evaluated from regions of interest taken from the high and low radioactive concentration regions. Due to the limited spatial resolution of the detection system used, it was considered necessary to define these regions of interest away from distribution boundaries. This was achieved by taking a narrow region of interest in the central part of the surrounding 100 kBq/ml region and a small square of 3 × 3 pixels in the 20 kBq/ml region at the center. The average number of events per pixel thus obtained were finally converted into radioactive concentration values using a calibration factor derived from a fairly large region of interest of respectively uncorrected and 1-D and 2-D scatter corrected transverse sections of the calibration measurement. The calculated radioactive concentrations are given separately for the high and low concentration regions and as a function of the axial extension of radionuclide distributions (Fig. 9). According to this figure, the calculated radioactive concentrations obtained without scatter correction are influenced by axial extensions of radioactive distributions and the concentrations of radioactivity in the neighborhood. This influence is marked in the values obtained from this low concentration region while these effects are small in the region of high concentration.

Measured concentrations were in better agreement with the true concentrations, when either the 1-D or the 2-D scatter correction technique was applied. The 1-D scatter correction, however, changes the calculated concentration values by the same amount, irrespective of the axial radioactive distribution. Fairly accurate results were still obtained in regions of high concentration, but in regions of low concentration accurate values were obtained only in distributions with axial dimensions comparable to the line source that was used to establish the 1-D scatter distribution function. The 2-D scatter correction, on the other hand corrects the values by an appropriate amount irrespective of the axial extension or the concentration of radioactivity in the neighborhood, thereby predicting concentration values in good agreement with the true concentration values.

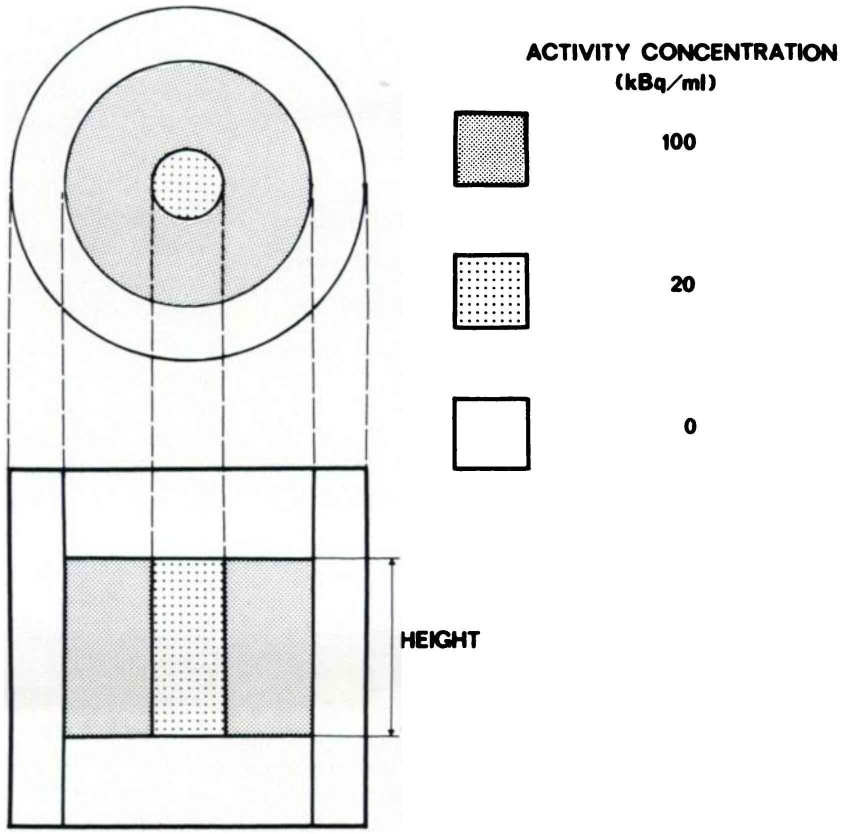

FIGURE 5
Top and lateral views of radioactive distributions used in SPECT studies with cylindrical phantom (diameter 200 mm). Measurements were performed with axial distributions of radioactivity varying from 25 mm to 100 mm.

CLINICAL EXAMINATIONS

Some clinical examples are presented in Figure 10 (liver/spleen examination using [^{99m}Tc] ALBU-RES, and Fig. 11 (regional brain blood-flow examination using [^{99m}Tc]HM-PAO).

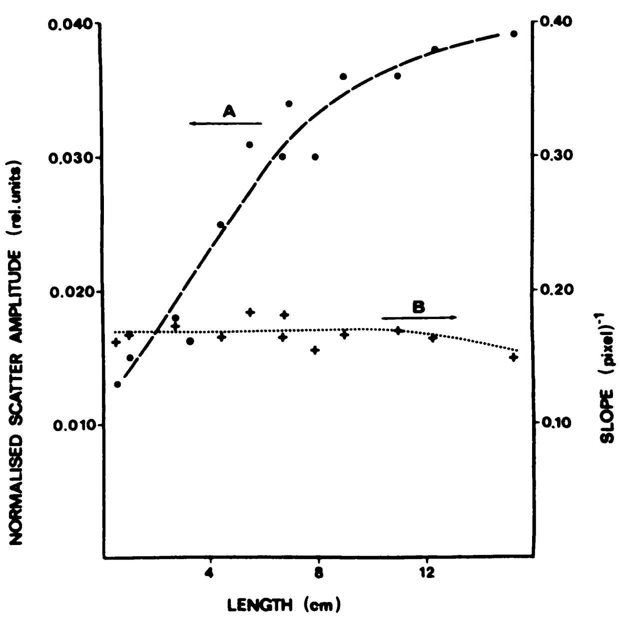

FIGURE 6
Dependence on amplitude (A) and slope (B) of the 1-D scatter distribution function f(x) = A exp (−Bx) from the length of the line source in data acquisition.

Two adjacent sections are presented for the liver/spleen examination. The transverse sections reconstructed from uncorrected projection data are presented in Figure 10A and C and the transverse sections reconstructed from scatter-corrected projection data are presented in Figure 10B and D. The improved contrast obtained by scatter correction is clearly seen and has been quantified by analysis of the regions 1 and 2 in an area corresponding to the liver metastasis and to normal liver tissue, respectively. The ratio of the average number of events/pixel between region 1 and 2 is 0.24 without and 0.04 with correction for scattered radiation.

A transverse section from a brain blood-flow examination is presented in the same way, with the section reconstructed from uncorrected projection data in Figure 11A and the section reconstructed from scatter corrected projection data in Figure 11B. Regions 1 and 2 were used to evaluate the ratio of the concentration of radioactivity in a region corresponding to gray matter (2) to the concentration in a region corresponding to white matter (and partly CSF space) (*1*). The ratio between the average number of events/pixel in regions 2 and 1 is 1.6 without scatter correction and 2.3 with correction for scattered radiation.

DISCUSSION

A primary aim of nuclear medicine examinations is to produce highly qualitative images with quantitative information about the radioactive concentration. This

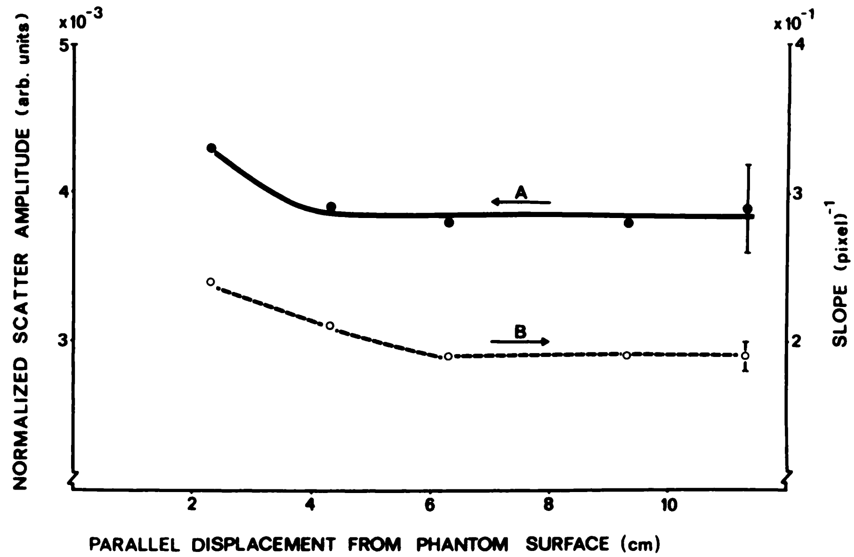

FIGURE 7
Amplitude—A (solid line) and slope—B (dashed line) of the 2-D scatter distribution function. Variation with displacement, from the surface of the phantom (diameter 220 mm), in a direction parallel to the collimator plane.

goal is hardly achieved without correction for the falsely positioned events resulting from scattered photons. Thus, quantification attempted without this correction will be seriously hampered by differences in scatter patterns between the actual and the calibration measurement. In the case of qualitative images where a calibration is not required, the observed patterns deteriorate image quality more in the central than the outer regions.

In a given radioactive distribution, the number of scattered events in a region with dimensions that are of the order of the mean free path or less of the interacting photons, will depend on the concentration in both the region itself and in the surroundings. A region of low radioactivity in the body, for instance, will contribute less scattered events to an adjacent region of higher radioactivity than in the case of a uniform high concentration in the whole body. On the other hand, the surrounding high radioactivity will lead to a higher number of scattered events in the region of low concentration than would be the case in a corresponding uniform distribution of low concentration.

This effect is, for instance, seen in Figure 9. The measured activity concentrations for uncorrected SPECT studies are based on a calibration value obtained from a uniform solution. Due to the presence of a low concentration region, the use of this calibration value will lead to prediction of values consistently lower than the actual (100 kBq/ml), in the region of high concentration. On the other hand, the predicted concentrations in the region of low concentration will be consistently higher than the actual 20 kBq/ml. In both regions, the predicted concentrations will gradually decrease as the axial distribution becomes shorter than the calibration (100 mm) due to lack of scatter contribution from distant radioactivity.

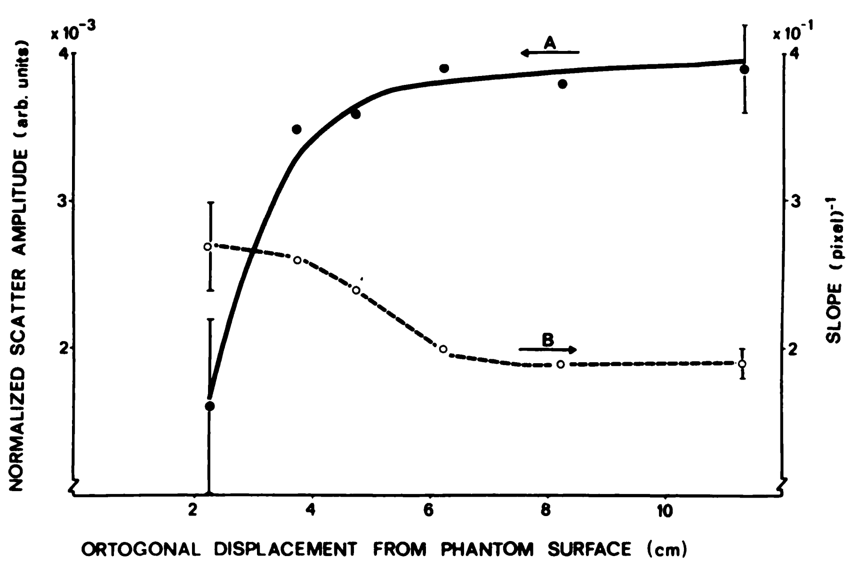

FIGURE 8
Amplitude—A (solid line) and slope—B (dashed line) of the 2-D scatter distribution function. Variation with displacement, from the surface of the phantom (diameter 220 mm), in a direction orthogonal to the collimator plane.

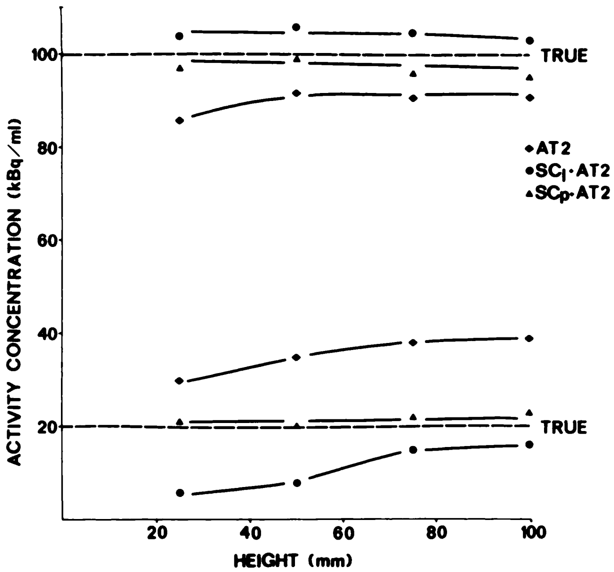

FIGURE 9
Measured concentration for different axial radioactive distribution without (♦—♦), with 1-D (●—●) and with 2-D (▲—▲) scatter correction. The actual radioactive concentrations (100 and 20 kBq/ml) are indicated horizontal dashed lines.

The implementation of both the 1-D and the 2-D scatter correction as they are used in this work posed some restrictions on these techniques. Any deviations of the scatter distribution function from the center function derived for a uniformly dense object were not accounted for in either technique. Furthermore, the dependence of the 1-D technique on source length in the axial direction was not accounted for either. While the 1-D scatter distribution function has been shown to be independent of position in a relatively large central region of phantoms (*14*) it depends on the axial source length. The validity of the 2-D scatter distribution function, on the other hand, does not depend on some specific source geometry (other than a point), and has been shown (Figs. 7 and 8) to be fairly independent of position, except in the surface region (30 mm from the phantom surface) where low values of scatter amplitude were recorded. This problem, which is inherent in both 1-D and 2-D scatter correction, was avoided in this work by conducting all SPECT measurements without surface activity (Fig. 5). In fact, this arrangement is comparable with most clinical situations since specific uptake of radioactive tracers close to the body surface are rare except in a few special applications such as in the facial skeleton. In these rare cases with superficial uptake, scatter correction may be conducted using a carefully chosen surface scatter function that is designed to suit the situation at hand.

Unlike the 2-D scatter correction technique, the 1-D technique relies entirely on the existence of a mixture of primary and scattered events in a section in which scatter saturation prevails. In this case, the 1-D scatter correction technique is unreliable in sections close to the upper or lower boundaries of radioactive distributions.

The 2-D scatter correction technique may therefore be used in a wider field of clinical applications. Since the use of the 2-D technique will produce a better

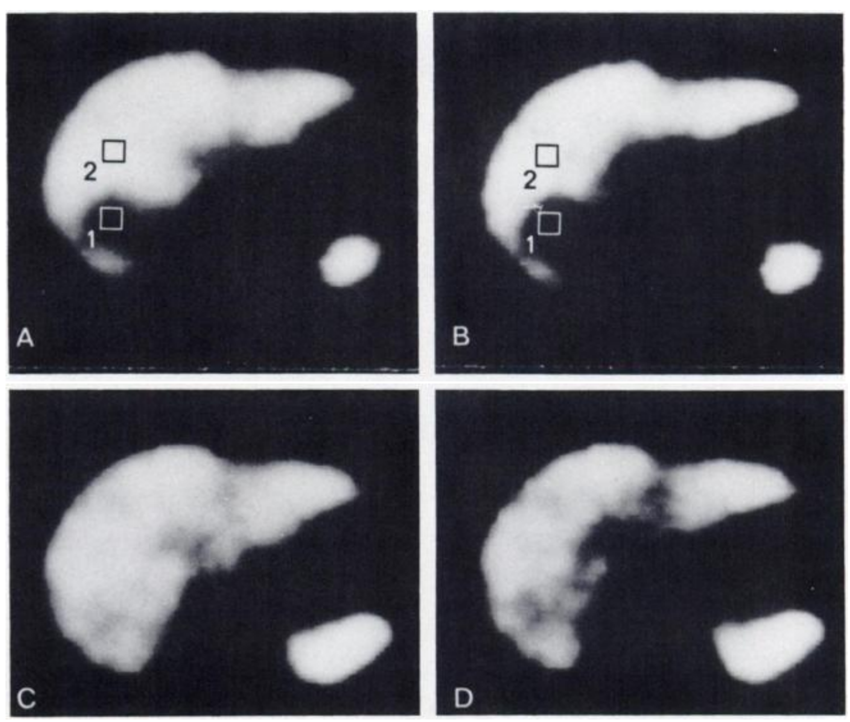

FIGURE 10
Liver/spleen examination using 120 MBq [^{99m}Tc]ALBU-RES. Two transverse sections, reconstructed without (A and C) and with (B and D) correction for scattered radiation, are shown. The ratio of the average number of events/pixel between region 1 and 2 is 0.24 without and 0.04 with correction for scattered radiation.

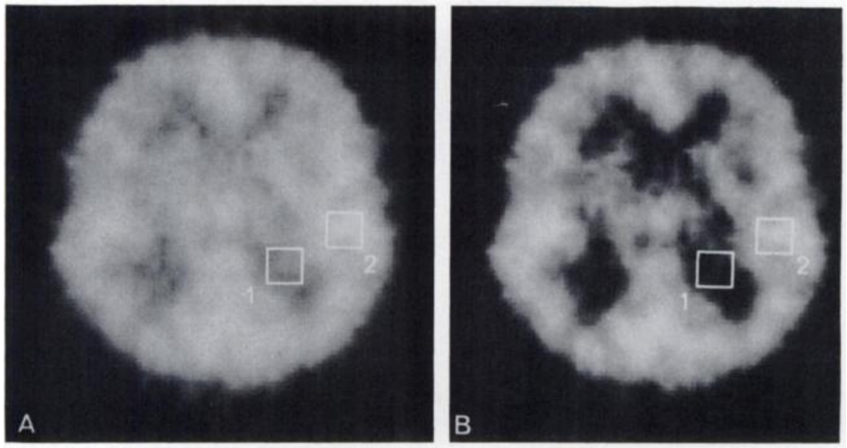

FIGURE 11
Brain blood-flow examination using 500 MBq [^{99m}Tc]HM-PAO. Transverse sections reconstructed without (A) and with (B) correction for scattered radiation are shown. The ratio of the average number of events/pixel between region 2 and 1 is 1.6 without and 2.3 with correction for scattered radiation.

estimate of the actual amount and distribution of recorded scattered events, it is more suitable for quantitative evaluation.

REFERENCES

1. Sanders TP, Sanders TD, Kuhl DE. Optimizing the window of an Anger camera for ^{99m}Tc. *J Nucl Med* 1971; 12:703–706.
2. Rollo FD, Schulz AG. Effect of pulse-height selection on lesion detection performance. *J Nucl Med* 1971; 12:690–696.
3. Egbert SD, May RS. An integral-transport method for Compton-scatter correction in emissioncomputed tomography. *IEEE Trans Nucl Sci* 1980; NS-27:543–548.
4. Beck JW, Jaszczak RJ, Coleman RE, et al. Analysis of SPECT including scatter and attenuation using sophisticated Monte Carlo modeling methods. *IEEE Trans Nucl Sci* 1982; NS-29:506–511.
5. Floyd CE, Jaszczak RJ, Harris CC, et al. Monte Carlo evaluation of Compton scatter subtraction in single photon emission computed tomography. *Med Phys* 1985; 12:776–778.
6. Floyd CE, Jaszczak RJ, Harris CC, et al. Energy and spatial distribution of multiple order Compton scatter in SPECT: a Monte Carlo investigation. *Phys Med Biol* 1984; 29:1217–1230.
7. Erhardt JC, Oberley LW. Effects of spectral changes on scanning. *Radiology* 1972; 104:207–208.
8. Bloch P, Sanders T. Reduction of the effects of scattered radiation on a sodium iodide imaging system. *J Nucl Med* 1973; 14:67–72.
9. Waggett DJ, Wilson BC. Improvement of scanner performance by subtraction of Compton scattering using multiple energy windows. *Br J Radiol* 1978; 51:1004–1010.
10. Jaszczak RJ, Coleman RE, Greer KL. The subtraction of scattered events from SPECT photopeak events [Abstract]. *J Nucl Med* 1983; 24:P82.
11. Bergström M, Eriksson L, Bohm C, et al. Corrections for scattered radiation in a ring detector positron camera by integral transformation of the projection. *J Comp Assist Tomogr* 1983; 7:42–50.
12. Axelsson B, Msaki P, Israelsson A. Subtraction of Compton-scattered photons in single emission computed tomography. *J Nucl Med* 1984; 25:490–494.
13. Floyd CE, Jaszczak RJ, Greer KL, et al. Deconvolution of Compton scatter in SPECT. *J Nucl Med* 1985; 26:403–408.
14. Axelsson B, Israelsson A, Larsson SA, et al. Attenuation and scatter correction aiming at quantitative SPECT. Proceedings 22nd International Annual Meeting of the Society of Nuclear Medicine-Europe, 23–26, 1984.
15. Msaki P, Axelsson B, Israelsson A, et al. An improved scatter correction technique in SPECT using point spread scatter function. Proceedings of the XIV International Conference on Medical and Biological Engineering and VII International Conference on Medical Physics Vol 23, Supplement Part 2, 1985.
16. Larsson SA. Gamma camera emission tomography, development and properties of a multi-sectional emission computer tomography system. *Acta Radiol* (supplement 363), 1980.
17. Hubbell JH. Photon cross sections, attenuation coefficients, and energy absorption coefficients from 10 keV to 100 GeV. Report NSRDS-NBS 29, 1969.
18. Dudgeon DE, Mersereay RM. Iterative implementations for 2-D IIR filters. In multidimensional digital signal processing. Prentice-Hall, 1984 pp 224–230.
19. Larsson SA, Axelsson B, Dahl LM, et al. The use of 1-D and 2-D scatter deconvolution techniques for contrast enhancement and quantification in SPECT. Proceedings of the 33rd Annual Meeting of the Society of Nuclear Medicine [Abstract]. *J Nucl Med* 1986; 27:P6.